In situ SEM/EDS compositional characterization of osteocytes and blood vessels in fossil and extant turtles on untreated bone surfaces; different preservational pathways microns away

Edwin-Alberto Cadena [Corresp. 1, 2]

[1] Facultad de Ciencias Naturales, Grupo de Investigación Paleontología Neotropical Tradicional y Molecular (PaleoNeo), Universidad del Rosario, Bogotá, Colombia

[2] Smithsonian Tropical Research Institute, Panama City, Panama

Corresponding Author: Edwin-Alberto Cadena
Email address: edwin.cadena@urosario.edu.co

Osteocytes and blood vessels are the main cellular and tissue components of the bone tissue of vertebrates. Evidence of these soft-tissue microstructures has been widely documented in the fossil record of Mesozoic and Cenozoic turtles. However, all these studies have characterized morphologically and elementally these microstructures via isolation from the fossilized bone matrix where they were preserved or in ground sections, which could raise skepticism about the results due to potential cross-contamination or reagents effects. Fossil turtle bones from three different localities with distinct preservation environments and geological settings, including *Mongolemys elegans* from the Late Cretaceous of Mongolia, *Allaeochelys crassesculpta* from the Eocene of Germany, and a podocnemidid indet. from the Miocene of Colombia are studied here. Bone from two extant turtle species, *Lepidochelys olivacea*, and *Podocnemis lewyana*, as well as a commercial chicken *Gallus gallus* were used for comparisons. Scanning Electron Microscopy-Energy Dispersive Spectroscopy analyses performed directly on untreated fresh surfaces show that osteocytes-like in the fossil turtle bone are mostly composed of iron and manganese. In contrast, the in situ blood vessels-like of the fossil turtles, as well as those from the extant taxa are rich in elements typically organic in origin (carbon and nitrogen), which are absent to minimally present in the surrounding bone or rock matrix; this suggests a possible endogenous composition for these fossil structures. Also, the results presented here show that although originally both (osteocytes and blood vessels) are organic soft components of bone as evidenced in the extant turtles and chicken, they can experience completely different preservational pathways only microns away from each other in the same fossil bone.

In situ SEM/EDS compositional characterization of osteocytes- and blood vessels-like in fossil and extant turtles on untreated bone surfaces; different preservational pathways microns away.

Edwin-Alberto Cadena[1,2]

[1] Facultad de Ciencias Naturales, Grupo de Investigación Paleontología Neotropical Tradicional y Molecular (PaleoNeo), Universidad del Rosario, Bogotá, Colombia
[2] Smithsonian Tropical Research Institute, Panama City, Panama

Corresponding Author:
Edwin-Alberto Cadena[1]
Cra 26 63b-48, Bogotá, 111221, Colombia
Email address: edwin.cadena@urosario.edu.co

Abstract

Osteocytes and blood vessels are the main cellular and tissue components of the bone tissue of vertebrates. Evidence of these soft-tissue microstructures has been widely documented in the fossil record of Mesozoic and Cenozoic turtles. However, all these studies have characterized morphologically and elementally these microstructures via isolation from the fossilized bone matrix where they were preserved or in ground sections, which could raise skepticism about the results due to potential cross-contamination or reagents effects. Fossil turtle bones from three different localities with distinct preservation environments and geological settings, including *Mongolemys elegans* from the Late Cretaceous of Mongolia, *Allaeochelys crassesculpta* from the Eocene of Germany, and a podocnemidid indet. from the Miocene of Colombia are studied here. Bone from two extant turtle species, *Lepidochelys olivacea* and *Podocnemis lewyana*, as well as a commercial chicken *Gallus gallus* were used for comparisons. Scanning Electron Microscopy-Energy Dispersive Spectroscopy analyses performed directly on untreated fresh surfaces show that osteocytes-like in the fossil turtle bone are mostly composed of iron and manganese. In contrast, the *in situ* blood vessels-like of the fossil turtles, as well as those from the extant taxa are rich in elements typically organic in origin (carbon and nitrogen), which are absent to minimally present in the surrounding bone or rock matrix; this suggests a possible endogenous composition for these fossil structures. Also, the results presented here show that although originally both (osteocytes and blood vessels) are organic soft components of bone as evidenced in the extant turtles and chicken, they can experience completely different preservational pathways only microns away from each other in the same fossil bone.

42 **Keywords:** Fossil cells, exceptional preservation, osteoblasts-like, Testudines, Deep time,
43 Mongolia, Colombia, Germany

44

Introduction

46

47 Bone is a complex biological tissue that characterizes extant and fossil vertebrates, and consists
48 of a mineralized (calcium, phosphorus) and a non-mineralized (collagen and non-collagenous
49 proteins) extracellular matrix, plus water and some lipids (Boskey & Gehron 2013; Rey et al.
50 2009). Cells involved in bone tissue are osteoclasts, osteoblasts, and the most abundant of them
51 osteocytes (Bonewald 2011). Osteocytes are embedded within the hard-mineralized component
52 of bone throughout life (exceptions being when released by fracture or during remodeling)
53 (Robling & Bonewald 2020), providing them high preservation potential within fossil bones,
54 which has been extensively documented in different clades of vertebrates (e.g., Bailleul et al.
55 2019; Enlow & Brown 1956; Pawlicki & Nowogrodzka-Zagorska 1998; Schweitzer 2011;
56 Schweitzer et al. 2013; Surmik et al. 2019). Similar preservation of osteocytes- and blood
57 vessels-like has also been documented in fossil turtles, showing that their preservation is
58 independent of geologic time, paleoenvironment, lithology, lineages, and latitude (Cadena 2016;
59 Cadena et al. 2013; Cadena & Schweitzer 2012, 2014)

60

61 Something in common to all aforementioned studies are the analytical tools used to study and
62 characterize these fossil bone microstructures, which include principally: 1) ground sections and
63 observation under transmitted and polarized microscopy (Cadena & Schweitzer 2012; Surmik et
64 al. 2019); 2) bone demineralization using ethylenediaminetetraacetic acid (EDTA) as a chelating
65 agent (0.5 M, pH 8.0), facilitating release the osteocytes-, blood vessels-, and any other cells- or
66 soft-tissue fibers-like from the bone matrix for their posterior study by transmitted and/or
67 polarized light, scanning and/or transmission electron microscopy and any coupled elemental
68 analyzer, Raman spectroscopy, Fourier-transform infrared spectroscopy (FTIR), immunological
69 and antibody studies (e.g., Alfonso-Rojas & Cadena 2020; Bailleul et al. 2019, 2020; Cadena
70 2016; Saitta et al. 2019; Schweitzer et al. 2013; Surmik et al. 2019; Wiemann et al. 2018)

71

72 The preservation of these soft-tissue microstructures (osteocytes and blood vessels) and their
73 potential original constituents (proteins and DNA) has been questioned and considered a
74 consequence of microbial interactions within fossil bone and its microenvironment or even as a
75 result of cross-contamination in the laboratory (Buckley et al. 2017; Kaye et al. 2008; Saitta et al.
76 2019). The 'biofilm hypothesis' as a source for soft-tissue preservation in dinosaur bones has
77 been rigorously tested, which identified fundamental morphological, chemical and textural
78 differences between the resultant biofilm structures and those derived from dinosaur bone,
79 demonstrating that the recovered microstructures in the reports cited above are endogenous in
80 origin and that the 'biofilm hypothesis' should therefore be rejected (Schweitzer et al. 2016).
81 Issues concerning cross-contamination and replications, timing of sample collections, and
82 reagents have also been addressed by Schweitzer et al (2019).

83

84 Compositionally, the osteocytes- and blood vessels-like from different clades of fossil
85 vertebrates have been shown to commonly be enriched in iron (Cadena 2016; Schweitzer et al.
86 2014; Surmik et al. 2019; Ullmann et al. 2019), an element that has been suggested to play a key
87 role in preserving and even masking identification of proteins in fossil tissues via Fenton

88   reactions (Schweitzer et al. 2014). Other elements typically found in these fossil bone
89   microstructures are carbon, calcium, and silicon (Cadena 2016; Ullmann et al. 2019). At present,
90   all these studies of elemental characterization have been conducted using SEM/EDS on isolated
91   (post-demineralization) osteocytes- and blood vessels-like, or from polished ground sections,
92   which implies some degree of manipulation or contact with reagents or preparation tools,
93   potentially raising skepticism on the elemental results.
94
95   Here, I explore the *in situ* (directly on fresh and untreated surfaces) preservation and elemental
96   composition of bone microstructural elements (cells and blood vessels) of fossil turtle bones
97   from three localities which have completely different geological settings (lithological,
98   taphonomic, and fossil diagenesis), including: 1) Gobi Desert, Mongolia, from the Late
99   Cretaceous (late Campanian–early Maastrichtian); 2) Messel Pit, Germany, from the Eocene; and
100   3) La Venta fauna, Colombia, from the Miocene. Comparison samples include bone from two
101   extant turtles and a domesticated chicken. I discuss herein the results of these analyses and the
102   advantages of using *in situ* SEM/EDS for understanding preservation of cells/tissues in fossils.
103

Materials & Methods

105
106   **Fossil and extant samples.** All the fossil and extant samples analyzed here were free of any
107   resin, glue, or stabilizing additives since field collection. Two small pieces donated by Dr. M.
108   Norell (American Museum of Natural History, AMNH) from a partially- articulated shell
109   (carapace and plastron) of *Mongolemys elegans* (IGM-90/42) were used for this study. Specimen
110   IGM-90/42 has been previously figured, including ground sections that show excellent
111   preservation of osteocytes-like under transmitted light microscopy (Cadena et al. 2013, figs. 7,
112   9). This fossil material was collected by the AMNH and the Mongolian Academy of Sciences
113   joint field expeditions at the Bugin Tsav locality, Gobi Desert, Mongolia, from fine-grained
114   sandstones representing ponds deposits within the Nemegt Formation, considered to be late
115   Campanian–early Maastrichtian (~ 80 Ma) in age (Jerzykiewicz 2000, references therein).
116
117   Small isolated fragments from the carapace of an *Allaeochelys crassesculpta* (SMF ME 2449)
118   were donated by Dr. K. Smith (Senckenberg Naturmuseum Frankfurt, SMF); these were
119   collected from the well-known locality of Messel Pit, which represents volcanically-influenced
120   lake deposits from the early-middle Eocene (~ 48 Ma) (Lenz et al. 2015). Osteocytes-, blood
121   vessels-, and collagen fibers-like from this specimen were previously described and elementally
122   characterized by Cadena (2016, figs, 4–7).
123
124   Carapace fragments from a podocnemidid indet. specimen, (UR-CP-0043), as well as the
125   surrounding rock matrix, were collected in 2018 directly from an excavation site (approximately
126   1.5 m from the surface) using strict aseptic techniques (nitrile gloves, face mask, wrapped in
127   sterilized aluminum foil and kept in glass containers with silica gel for moisture control until
128   analyses were performed). This fossil material was collected from the Repartidora locality, La
129   Victoria Formation, middle Miocene (13.6 ± 0.2 Ma), Tatacoa Desert, Colombia, from what are
130   interpreted as fluvial deposits (Cadena et al. 2020). Permits for collecting and study of the
131   samples were granted by the Colombian Geological Survey (Radicado N° 20193800017321).
132

133 For comparisons, two extant turtle carcasses were sampled directly in the field following the
134 same aseptic protocols used for specimen UR-CP-0043. The first corresponds to carapace
135 fragments from an individual of the sea turtle *Lepidochelys olivacea* (uncatalogued specimen)
136 collected in January 2017 at the Pacific coast, Santa Elena Province, Ecuador, permit granted by
137 Yachay Tech University. The second (uncatalogued specimen) sampled corresponds to a carcass
138 of the side-necked turtle *Podocnemis lewyana* found in a sand bed of the Magdalena River, close
139 to La Victoria village, Huila Department, Colombia, under a permit granted by the ethics
140 committee of Universidad del Rosario (Resolución DVO005 672-CV1066) and the Colombian
141 Autoridad Nacional de Licencias Ambientales (Technical concept Nº 02263, 2019). A third
142 sample corresponds to a femur fragment from a commercial chicken *Gallus gallus* obtained
143 directly from a local market. Muscle tissue was removed and small bone fragments were cut
144 using a sterilized scalpel and dried out at room temperature for several days.
145

146 **Institutional abbreviations.** AMNH, American Museum of Natural History, New York, USA;
147 IGM, Geological Institute of the Mongolian Academy of Sciences, Ulaan Baatar, Mongolia;
148 SMF ME, Senckenberg Naturmuseum Frankfurt, Germany; UR-CP, paleontological collection,
149 Facultad de Ciencias Naturales, Universidad del Rosario, Bogotá, Colombia.
150

151 **Scanning electron microscopy and elemental analysis (SEM/EDS).** Each of the fossils, rock
152 matrix and extant bone samples were placed between two disposable sterilized lab-weighing
153 boats and gently hit with a rock hammer to break them into smaller pieces. Using tweezers
154 (sterilized before every mounting process) one of the smaller pieces of broken bone was
155 transferred to an SEM holder with adjustable screws and secured. To prevent any potential
156 particles or dust from entering the SEM chamber, each sample was gently air cleaned before
157 placing it in the SEM carousel. Elemental analysis was performed in combination with high
158 resolution imaging of the bone surfaces, as well as (in some cases) the rock matrix attached to it
159 using a scanning electron microscope coupled with an energy-dispersive X-ray spectroscopy
160 analyzer (Phenom ProX, at the Paleontological Lab of Yachay Tech University (YTU), San
161 Miguel de Urcuqui, Ecuador). Imaging was performed at 5 kV using different magnification
162 settings, and point-and-map analyses of elemental composition of selected regions or features
163 were performed at 15 kV. At least five or more points were explored for each osteocyte- or blood
164 vessel-like, as well as the surrounding bone matrix or rock. Quality of EDS analyses was
165 evaluated considering only those with one million counts or higher. Full raw data is presented in
166 Data S1.
167

168 **Bone demineralization.** In order to test for the occurrence and preservation of osteocytes- and
169 blood vessels-like in some of the samples, small bone pieces of *Mongolemys elegans* (IGM-
170 90/42) and the podocnemidid indet. specimen (UR-CP-0043) were demineralized using disodium
171 ethylenediaminetetraacetic acid (EDTA) (0.5 M, pH 8.0 filter-sterilized using a 0.22 μm filter) as
172 previously described (Cadena 2016; Cleland et al. 2015) for a period of five days to two weeks,
173 or until osteocytes- and blood vessels-like were detected. Photographs of the recovered
174 osteocytes-like were taken using a transmitted light microscope (Olympus BX-63) and a
175 polarized light microscope (Olympus BX-53) at the paleontological lab of YTU. Some of the
176 isolated osteocytes-like from IGM-90/42 were collected with a tip in a 1.5 ml tube, rinsed three
177 times with E-pure water to get rid of EDTA, being centrifuged at 1500 RPM for 2 minutes
178 between step. A drop of the supernatant was mounted in a stub, dried out at room temperature

179   inside in a sealed small SEM-stub box to avoid any air or dust particles interact with the sample,
180   and analyzed following the same protocol and SEM/EDS machine aforementioned.
181

Results

183

184   ***Mongolemys elegans,*** **Late Cretaceous of Mongolia.** The *in situ* osteocytes-like of *Mongolemys*
185   *elegans* (IGM-90/42) under SEM exhibit a distinct contrast with the surrounding bone matrix,
186   which is exclusive of their three-dimensional volume, and it is also different from the empty
187   osteocytes-lacuna, which exhibits the same contrast as the bone matrix (Figs. 1A–B).
188   Compositionally, they are predominantly composed of iron, calcium, carbon, manganese, and
189   minor amounts of barium and nitrogen (Figs. 1C–K; 2A; Data S2; and Fig. S1). There is no
190   evidence of any of these elements in empty osteocyte-lacunae walls, which are composed of
191   calcium and phosphorus, like the bone matrix (Figs. 1L–N). The isolated osteocytes-like show
192   that iron is concentrated on their external surface and the manganese in the internal, this is
193   clearly evident in elemental maps and a cross-line elemental profile (Figs. 1O–P; S1).
194   Observation of some of the isolated (post-demineralization) osteocytes-like under transmitted
195   and polarized light revealed excellent morphological preservation, with some of them emitting
196   low-degree birefringence colors under polarized light (Fig. 3).
197

198   ***Allaeochelys crassesculpta,*** **Eocene of Germany.** The most abundant bone microstructures
199   preserved in this sample are blood vessels-like and the walls that formed the Haversian-
200   Volkmann (H-V) canals; also, in some, there is evidence of very small (2.5 μm diameter)
201   structures with a striated margin which resemble the morphology of osteoblast cells (Figs. 4A–D;
202   S2). The blood vessels-like exhibit a width of 1–3 μm, with an average wall thickness of 0.2 μm
203   (Fig. 4D). Compositionally, the blood vessels-like are mainly composed of carbon and nitrogen,
204   with minor amounts of calcium, phosphorus and iron (Figs. 2B; 4E–G; 4J–N; S2; Data S2). The
205   bone matrix surrounding them lacks nitrogen and carbon, and it is exclusively characterized by
206   calcium, phosphorus, and iron (Figs. 4E,I). A bone sample with rock matrix attached shows that
207   the bone is composed of calcium, phosphorus, iron, and nitrogen, and, in contrast, the rock
208   matrix is rich in aluminum and silicon (Figs. 2C–D; 4O–Q; Data S2).
209

210   **Podocnemidid indet, Miocene of Colombia.** The sample of the side-necked turtle from La
211   Venta, Colombia, shows on the bone external cortex preservation of walls that formed the H-V
212   canals, blood vessels- and osteocytes-like tightly embedded in the very homogenous bone matrix
213   (Figs. 5A–B; 5F–G). Elementally, the blood vessels-like and H-V canal walls are rich in carbon,
214   nitrogen, and calcium, with minor amounts of phosphorous and silicon (Figs. 2B; 5C–D; 5H–I;
215   Data S2). In contrast, the osteocytes-like are composed of iron, calcium, aluminum, manganese,
216   phosphorus, and minor amounts of silicon (Figs. 2B; 5H–J; Data S2). The bone matrix lacks
217   carbon and nitrogen, and it is constituted by calcium and phosphorus mainly (Figs. 2C; 5C, E,
218   H). An isolated bone fragment (post-demineralization) shows some of the osteocytes-like still
219   embedded in the matrix, varying in color from orange to black, the darker ones located closer to
220   black, dendritic mats (Figs. 5K–M).
221

222   ***In situ*** **extant turtle and chicken bone microstructures.** The carapace bone fragment of the
223   extant side-necked turtle *Podocnemis lewyana* shows osteocytes within lacunae (Figs. 6A–B).
224   Their composition is rich in carbon, nitrogen, calcium, and phosphorus (Figs. 2A; 6C–D; Data

225   S2). The bone matrix is relatively richer in calcium (Figs. 2C; 6C, E). The H-V canals exhibit a
226   distinct wall and a high concentration of blood vessels and red blood cells, which are rich in
227   carbon and nitrogen (Figs. 2B; 6F–G; S3; S4; Data S2). Similar spatial patterns and composition
228   are shared by the bone of the extant marine turtle *Lepidochelys olivacea* (Figs. 2; 6H–M; Data
229   S2), and the bone of *Gallus gallus* (chicken) (Figs. 2; 6N–P; Data S2).
230

Discussion

232

233   As previously shown (Cadena 2016; Schweitzer et al. 2014; Surmik et al. 2019; Ullmann et al.
234   2019), the *in situ* analyses presented here, concur with that iron is a very common constituent of
235   fossil osteocytes-like, such as those found in the Late Cretaceous *Mongolemys elegans* and the
236   Miocene podocnemidid indet. bone samples studied herein (Figs. 1,5). However, this
237   composition is not always homogenous and may vary between the external and the internal layer
238   of osteocytes-like, as shown in a broken and folded osteocyte-like from *M. elegans*, which
239   exhibits richer content of manganese internally and iron externally (Figs. 1O–P). High levels of
240   manganese were also detected in osteocytes-like from the Miocene side-necked turtle from
241   Colombia, indicating that besides iron as initially suggested by Schweitzer et al. (2014),
242   manganese may also be involved in the preservation of these bone microstructures in deep time.
243   The source for this rich content of manganese seems to be from manganese oxides such as
244   pyrolusite penetrating bone microfractures, which were found herein in some fragments of the
245   Miocene podocnemidid indet. from Colombia (Figs. 5K–M), and also has been characterized to
246   occur in dinosaur fossil bones from the same Nemegt Formation, from which the *M. elegans*
247   studied herein was collected (Owocki et al. 2016). The color variation exhibited by the fossil
248   osteocytes-like of *M. elegans* and podocnemidid indet. seems to be related to enrichment of
249   manganese, higher their manganese content darker their color. In contrast to the osteocytes of the
250   extant turtle and chicken bone, which are rich in carbon and nitrogen (Figs. 2, 6), these elements
251   only appear in minor amounts in fossil osteocytes-like. However, these cells exhibited a very
252   distinct composition when compared to the surrounding bone matrix and even the wall surfaces
253   of their osteocytes-lacunae, indicating that their mineralized preservation occurred at micro-scale
254   inside the bone, a hypothesis that should be tested by future studies using additional tools (e.g,
255   Raman and FTIR spectroscopy).
256

257   The blood vessels-l and H-V canal walls-like preserved in the Eocene *Allaeochelys crassesculpta*
258   from the Messel Pit and the Miocene podocnemidid indet. specimen from the La Venta not only
259   exhibited a similar morphology, but also exhibited the same elemental composition as their
260   corresponding tissues in extant turtle and chicken bone. (Figs. 2, 4, 5, S2, S3, S4; Data S2). In
261   both cases (extant and fossils) being rich in carbon and nitrogen, and differing from the
262   surrounding bone matrix which is richer in calcium and phosphorus, or the rock matrix which is
263   rich in silicon and aluminum (without any traces of carbon, calcium, or nitrogen) which suggests
264   that carbonates or nitrates were in the surrounding microenvironment. The *in situ* measurements
265   performed on some of the preserved blood vessels-like from *A. crassesculpta*, exhibiting uniform
266   fabric and thin walls of 0.2 µm thickness (Fig. 4D) suggest that they are not consistent with the
267   characteristics of biofilms, which tend to be amorphous and larger in diameter (Schweitzer et al.
268   2016). Blood vessels constitute one of the most promising microstructures preserved in fossil
269   turtles for molecular paleontology studies, and future studies should focus on their molecular *in*
270   *situ* characterization using ToF-SIMS mass spectrometry, similarly as it has been used in

271 dinosaurs and other fossil vertebrates (Alfonso-Rojas & Cadena 2020; Henss et al. 2013;
272 Lindgren et al. 2018; Schweitzer et al. 2019).
273
274 For the first time, I herein report the preservation of osteoblasts-like in fossil vertebrates,
275 particularly in the Messel Pit turtle *A. crassesculpta.* They occur as oval objects with striated
276 margins that are attached to the H-V canals (Figs. 5B–D; S2), and thus resemble the morphology
277 and size of osteblasts observed in electron micrographs of human bone (Nakamura 2007;
278 Schmidt et al. 2002). At the same time, evidence here provided from the Miocene podocnemidid
279 indet. turtle from Colombia (Figs. 5F–J) shows that, in the same bone specimen, osteocytes- and
280 blood vessels-like that are only 20 microns away from each other are compositionally different.
281 This indicates that each microstructure went through a different preservational pathway.
282 Osteocytes-like seem to be more mineralized than blood vessels-like in these fossil samples, with
283 high amount of iron and manganese, and less organic components than blood vessels-like (Fig. 2,
284 3). In the extant bone of turtles and chicken, osteocytes and blood vessels exhibit similar
285 elemental composition under SEM/EDS, both being rich in carbon and nitrogen, which are
286 typically present in abundance within proteins (Torabizadeh 2011) (Figs. 2, 6). A similar
287 composition was detected herein in fossil blood vessels from *A. crassesculpta* and the
288 podocnemidid indet., from Colombia (Figs. 4, 5).
289
290 Traditionally, it has been suggested that SEM/EDS has to be performed on homogenous or
291 polished surfaces to avoid topographic effects on EDS analyses (Goldstein et al. 2003).
292 However, as I showed here, such effects were negligible for the analyzed sample with
293 composition and signal intensities being very similar in both the fossil and extant samples (Fig.
294 2). I therefore suggest that a more critical condition for EDS analysis on untreated samples is
295 acquire the highest maximum count rate possible; above 1 million counts is ideal.
296

Conclusion

298
299 This study provided evidence that *in situ* analyses using a conventional technique, SEM/EDS, on
300 untreated fresh surfaces of fossil and extant bones constitutes a protocol that should be added to
301 the rigorous plethora of proxies and tools (e.g, those recently reviewed and summarized by
302 Schweitzer et al., (2019)) to support and demonstrate the preservation of cells, soft-tissues and
303 their original constituents in deep time. Furthermore, *in situ* analyses of fossil and extant bone
304 samples may also help eliminate any potential skepticism of results obtained by molecular
305 paleontology studies, because, as demonstrate here, it requires minimal sample
306 preparation/manipulation, use of reagents, or contact with lab tools that could cause possible
307 contamination.
308

Acknowledgements

310
311 I thank M. Norell, K. Smith, S. Schaal and A. Vanegas for access to samples. I also thank M.
312 Schweitzer for some preliminary feedback on some of the results presented here. Thanks are also
313 extended to Yachay Tech and the Colombian Geological Survey and Ethics Committee at
314 Universidad del Rosario for the permits to collect and analyze the samples. Thanks to P.
315 Ullmann and another anonymous reviewer for comments that improved this manuscript.

316

References

318

319 Alfonso-Rojas AF, and Cadena EA. 2020. Exceptionally preserved 'skin' in an Early Cretaceous fish
320   from Colombia. *PeerJ* 8:e9479.
321 Bailleul AM, O'Connor J, and Schweitzer MH. 2019. Dinosaur paleohistology: review, trends and new
322   avenues of investigation. *PeerJ* 7:e7764.
323 Bailleul AM, Zheng W, Horner JR, Hall BK, Holliday CM, and Schweitzer MH. 2020. Evidence of
324   proteins, chromosomes and chemical markers of DNA in exceptionally preserved dinosaur
325   cartilage. *National Science Review* 0. DOI:10.1093/nsr/nwz206.
326 Bonewald LF. 2011. The amazing osteocyte. *Journal of Bone Mineral Research* 26:229–238.
327 Boskey AL, and Gehron PR. 2013. The composition of bone. In: Rosen CJ, ed. *Primer on the metabolic*
328   *bone diseases and disorders of mineral metabolism*: John Wiley & Sons, Inc, 49–58.
329 Buckley M, Warwood S, van Dongen B, Kitchener AC, and Manning PL. 2017. A fossil protein chimera;
330   difficulties in discriminating dinosaur peptide sequences from modern cross-contamination. *Proc*
331   *Biol Sci* 284: 20170544. DOI.org/10.1098/rspb.2017.0544.
332 Cadena E. 2016. Microscopical and elemental FESEM and Phenom ProX-SEM-EDS analysis of
333   osteocyte-and blood vessel-like microstructures obtained from fossil vertebrates of the Eocene
334   Messel Pit, Germany. *PeerJ* 4:e1618.
335 Cadena EA, Ksepka DT, and Norell MA. 2013. New material of *Mongolemys elegans* Khosatzky and
336   Mlynarski, 1971 (Testudines: Lindholmemydidae), from the Late Cretaceous of Mongolia with
337   comments on bone histology and phylogeny. *American Museum Novitates* 3766:1–27.
338 Cadena EA, and Schweitzer MH. 2012. Variation in osteocytes morphology vs bone type in turtle shell
339   and their exceptional preservation from the Jurassic to the present. *Bone* 51:614–620.
340 Cadena EA, and Schweitzer MH. 2014. A pelomedusoid turtle from the Paleocene–Eocene of Colombia
341   exhibiting preservation of blood vessels and osteocytes. *Journal of Herpetology* 48:461–465.
342 Cadena EA, Vanegas A, Jaramillo C, Cottle JM, and Johnson TA. 2020. A new Miocene turtle from
343   Colombia sheds light on the evolutionary history of the extant genus *Mesoclemmys* Gay, 1873.
344   *Journal of Vertebrate Paleontology*. DOI:10.1080/02724634.2019.1716777.
345 Cleland TP, Schroeter ER, Zamdborg L, Zheng W, Lee JE, Tran JC, Bern M, Duncan MB, Lebleu VS,
346   and Ahlf DR. 2015. Mass spectrometry and antibody-based characterization of blood vessels
347   from Brachylophosaurus canadensis. *Journal of proteome research* 14:5252–5262.
348 Enlow DH, and Brown SO. 1956. A comparative histological study of fossil and recent bone tissues.
349   *Texas Journal of Science* 8:405–443.
350 Goldstein J, Newburry D, Joy D, Lyman C, Ehclin P, Lifshin E, Sawyer L, and Michael J. 2003. *Scanning*
351   *Electron Microscopy and X-Ray microanalysis*: Springer Science.
352 Henss A, Rohnke M, El Khassawna T, Govindarajan P, Schlewitz G, Heiss C, and Janek J. 2013.
353   Applicability of ToF-SIMS for monitoring compositional changes in bone in a long-term animal
354   model. *Journal of The Royal Society Interface* 10:20130332.
355 Jerzykiewicz T. 2000. Lithostratigraphy and sedimentary setting of the Cretaceous dinosaur beds of
356   Mongolia. In: Benton MJ, ed. *The age of dinosaurs in Russia and Mongolia*. Cambridge:
357   Cambridge University Press, 279–296.
358 Kaye TG, Gaugler G, and Sawlowicz Z. 2008. Dinosaurian soft tissues interpreted as bacterial biofilms.
359   *PLoS One* 3:e2808.
360 Lenz OK, Wilde V, Mertz DF, and Riegel W. 2015. New palynology-based astronomical and revised
361   40Ar/39Ar ages for the Eocene maar lake of Messel. *International Journal of Earth Sciences*
362   104:873–889.
363 Lindgren J, Sjövall P, Thiel V, Zheng W, Ito S, Wakamatsu K, Hauff R, Kear BP, Engdahl A, and
364   Alwmark C. 2018. Soft-tissue evidence for homeothermy and crypsis in a Jurassic ichthyosaur.
365   *Nature* 564:359–365.

366 Nakamura H. 2007. Morphology, function and differentiation of bone cells. *Journal of Hard Tissue*
367   *Biology* 16:15–22.
368 Owocki K, Kremer B, Wrzosek B, Krolikowska A, and Kazmierczak J. 2016. Fungal Ferromanganese
369   Mineralisation in Cretaceous Dinosaur Bones from the Gobi Desert, Mongolia. *PLoS One*
370   11:e0146293.
371 Pawlicki R, and Nowogrodzka-Zagorska M. 1998. Blood vessels and red blood cells preserved in
372   dinosaur bones. *Annales of Anatomy* 180:73–77.
373 Rey C, Combes C, Drouet C, and Glimcher MJ. 2009. Bone mineral: update on chemical composition and
374   structure. *Osteoporos International* 20:1013–1021.
375 Robling AG, and Bonewald LF. 2020. The Osteocyte: New Insights. *Annual Review of Physiol*ogy
376   82:485–506.
377 Saitta ET, Liang R, Lau MC, Brown CM, Longrich NR, Kaye TG, Novak BJ, Salzberg SL, Norell MA,
378   Abbott GD, Dickinson MR, Vinther J, Bull ID, Brooker RA, Martin P, Donohoe P, Knowles TD,
379   Penkman KE, and Onstott T. 2019. Cretaceous dinosaur bone contains recent organic material
380   and provides an environment conducive to microbial communities. *Elife* 8:e46205.
381 Schmidt C, Kaspar D, Sarkar MR, Claes LE, and Ignatius AA. 2002. A scanning electron microscopy
382   study of human osteoblast morphology on five orthopedic metals. *Journal of Biomedical*
383   *Materials Research* 63:252–261.
384 Schweitzer MH. 2011. Soft tissue preservation in terrestrial Mesozoic vertebrates. *Annual Review of*
385   *Earth and Planetary Sciences* 39:187–216.
386 Schweitzer MH, Moyer AE, and Zheng W. 2016. Testing the hypothesis of biofilm as a source for soft
387   tissue and cell-like structures preserved in dinosaur bone. *PLoS One* 11:e0150238.
388 Schweitzer MH, Schroeter ER, Cleland TP, and Zheng W. 2019. Paleoproteomics of Mesozoic Dinosaurs
389   and Other Mesozoic Fossils. *Proteomics* 19:e1800251.
390 Schweitzer MH, Zheng W, Cleland TP, and Bern M. 2013. Molecular analyses of dinosaur osteocytes
391   support the presence of endogenous molecules. *Bone* 52:414–423.
392 Schweitzer MH, Zheng W, Cleland TP, Goodwin MB, Boatman E, Theil E, Marcus MA, and Fakra SC.
393   2014. A role for iron and oxygen chemistry in preserving soft tissues, cells and molecules from
394   deep time. *Proceedings of the Royal Society B: Biological Sciences* 281:20132741.
395 Surmik D, Dulski M, Kremer B, Szade J, and Pawlicki R. 2019. Iron-mediated deep-time preservation of
396   osteocytes in a Middle Triassic reptile bone. *Historical Biology*.
397   DOI.org/10.1080/08912963.2019.1599884.
398 Torabizadeh H. 2011. All proteins have a basic molecular formula. *World Academy of Science,*
399   *Engineering and Technology* 54:961–985.
400 Ullmann PV, Pandya SH, and Ne llermoe R. 2019. Patterns of soft tissue and cellular preservation in
401   relation to fossil bone tissue structure and overburden depth at the Standing Rock Hadrosaur Site,
402   Maastrichtian Hell Creek Formation, South Dakota, USA. *Cretaceous Research* 99:1–13.
403 Wiemann J, Fabbri M, Yang T-R, Stein K, Sander PM, Norell MA, and Briggs DE. 2018. Fossilization
404   transforms vertebrate hard tissue proteins into N-heterocyclic polymers. *Nature Communications*
405   9:4741.
406
407

Figure 1

Figure 1. SEM/EDS analyses of *Mongolemys elegans* (IGM-90/42) bone.

(A) Micrograph of one of the osteocytes-like and an empty lacuna nearby. (B) EDS of the bone region shown in (A), in which orange indicates bone matrix (calcium), and blue-yellow denotes the osteocyte-like (oxygen and iron respectively). (C) Micrograph of one osteocyte-like, indicating the regions where EDS mapping and point analyses were performed. (D–E) Composite elemental map (D) and individual element maps (E) for the rectangle labeled as 1 in (C), in which osteocytes-like show high amount of iron and nitrogen. (F) Elemental point values of point 7 (bone matrix) shown in (C). (G) Elemental intensities for point 4 (osteocyte-like) shown in (C). (H) Micrograph of a broken osteocyte-like inside its lacuna. (I) Individual elements maps from rectangle 1 shown in (H), with the broken osteocyte-like showing a high content of manganese. (J) Elemental intensities for point 2 (bone matrix) shown in (H). (K) Elemental intensities for point 6 (osteocyte-like) shown in (H). (L) Micrograph of a empty lacuna. (M–N) Composite elemental map and individual elements maps for the rectangle labeled as 1 in (L), in which the wall surface of the lacuna exhibits the same composition as the bone matrix. (O) An isolated, broken, and folded osteocyte-like showing a high amount of iron at its external surface and manganese in its internal region, the red line denotes the cross-line described in (P). (P) Cross-line elemental profile across the broken and folded osteocyte-like shown in (O), revealing a switch between iron and manganese content between its external and internal surfaces. Full EDS results for the points shown in (C, H, and L) are presented in Fig. 2 and Data S2.
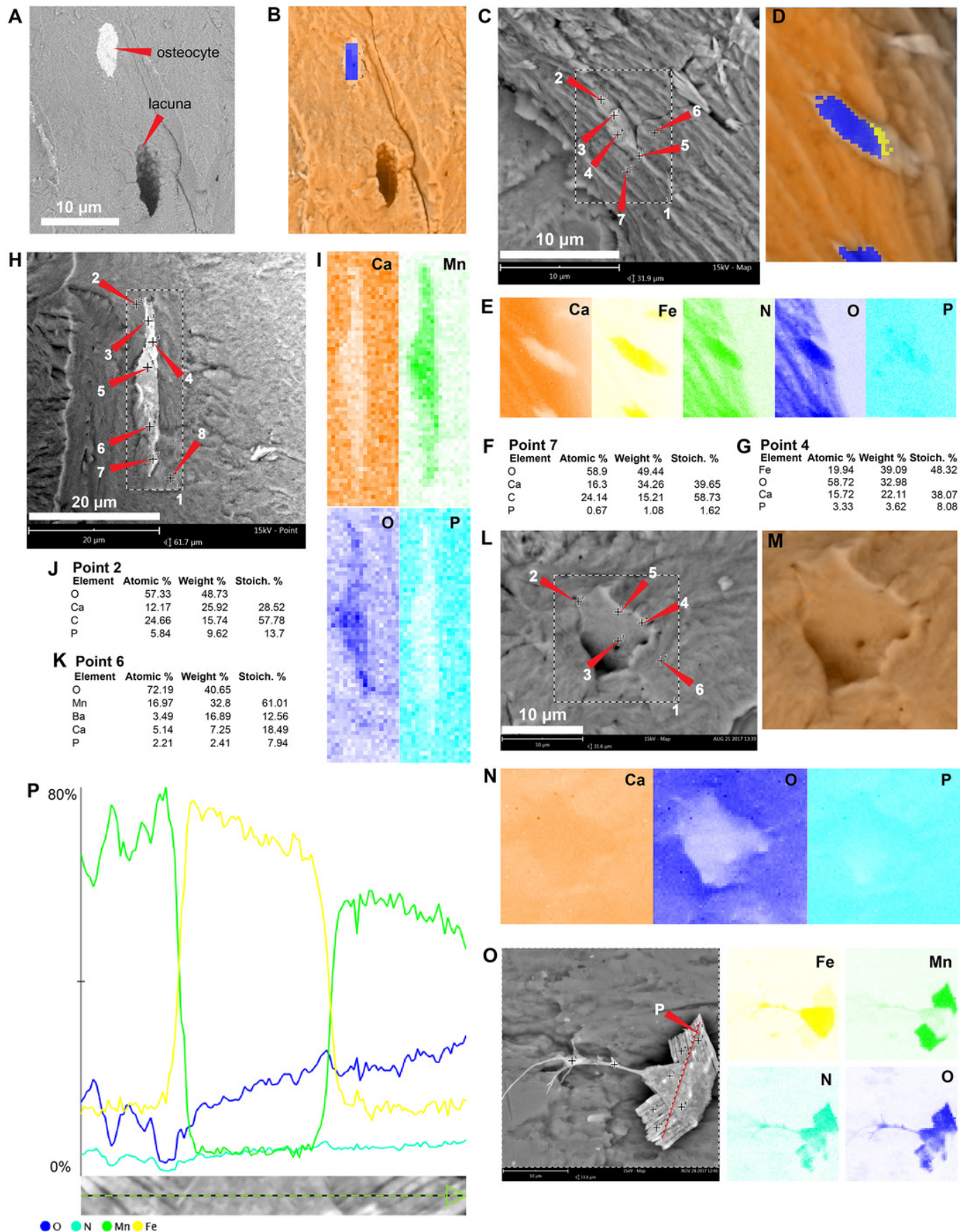
Figure 2

Figure 2. %Wt of elements for fossil and extant turtle bone

(A) EDS point analyses of osteocytes, indicating high amounts of iron and manganese in the fossil cells (from *Mongolemys elegans* and the podocnemidid indet. specimens), whereas carbon and nitrogen dominate the cells from extant taxa (*Podocnemis lewyana* and *Lepidochelys olivacea*), including those from a chicken (*Gallus gallus*). (B) EDS point analyses of blood vessels, with fossil and extant showing a similar elemental composition rich in carbon and nitrogen. (C) EDS point analyses of the bone matrix surrounding osteocytes or blood vessels. Note how fossil and extant samples exhibit similar %Wt values for calcium, carbon, and phosphorus. Fossils show relative enrichment in iron and a lower amount of nitrogen in comparison to the extant bone matrix samples. (D) EDS point analyses of the surrounding rock matrix, which show an absence of carbon, calcium, and nitrogen, but abundant silicon and aluminum. Full data for these EDS point analyses are presented in Data S1, S2.

A osteocytes

B blood vessels

C bone matrix

D rock

%Wt (weight percetange concentration)

Ca C N P Fe Mn

Ca C N P Fe

Ca C N P Fe

P Fe Si Al Mn

Fossils
- 🔴 *Mongolemys elegans*
- 🟠 Podocnemidid indt.
- 🟡 *Allaeochelys crassesculpta*

Extants
- 🔵 *Podocnemis lewyana*
- 🔵 *Lepidochelys olivacea*
- 🔵 *Gallus gallus*
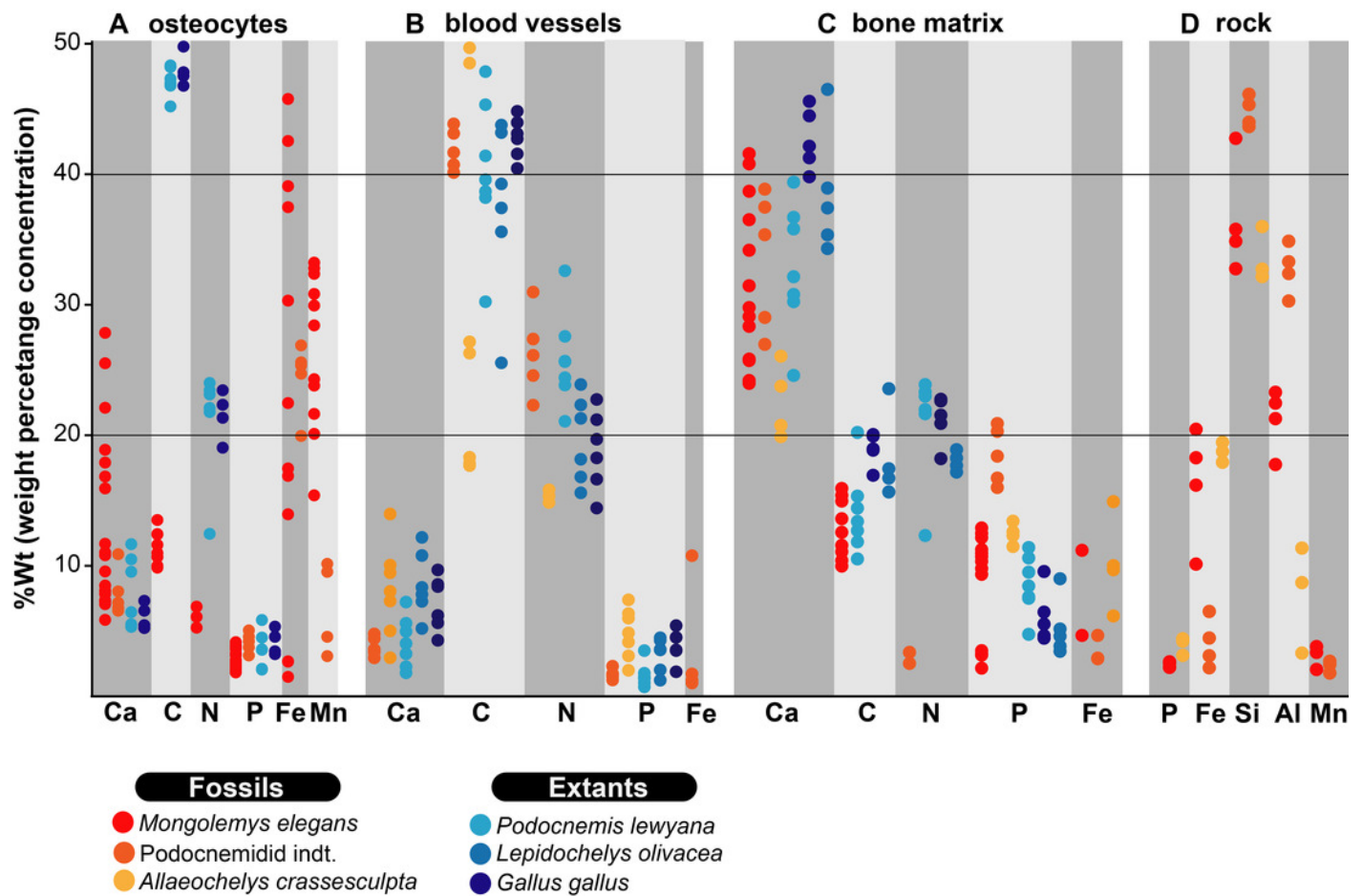
Figure 3

Figure 3. Fossil osteocytes-like from *Mongolemys elegans* (IGM-90/42).

(A–F) Isolated (post-demineralization) osteocytes-like viewed under transmitted light microscopy (A, C, E) and polarized light microscopy (B, D, F), showing low to moderate birefringence. All photographs taken with a 100X-oil immersion objective lens.
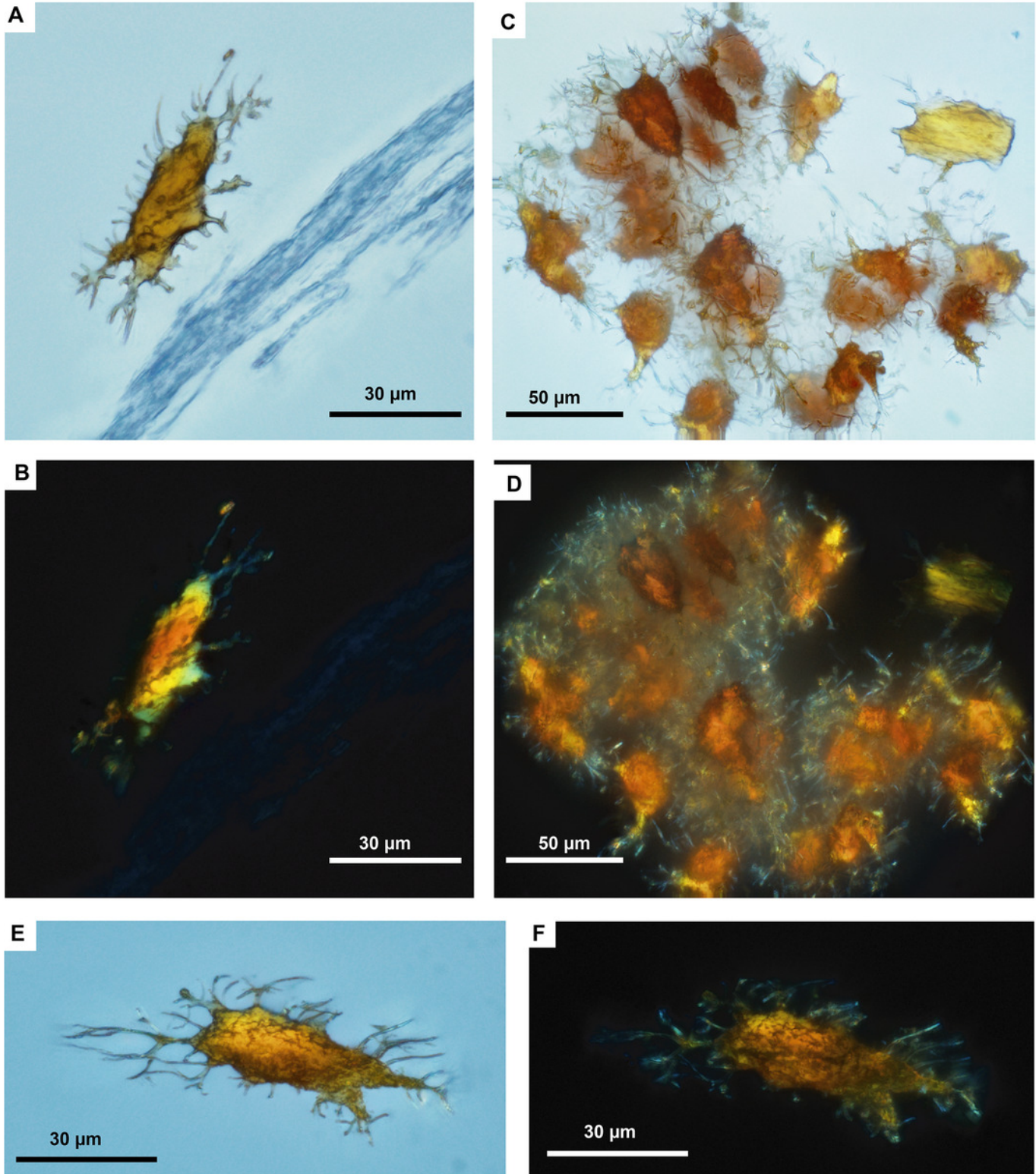
Figure 4

Figure 4. SEM/EDS analyses of *Allaeochelys crassesculpta* (SMF ME 2449) bone

(A–D) Micrographs of two Haversian canals, in which (B, D) show the blood vessels-like outlined in red, and osteoblasts-like outlined in green in. Measurements of the width of a blood vessel-like width, wall thickness, and osteoblast-like diameters are shown in (D). (E–G) Micrograph (E) and EDS elemental maps (F–G) of one of the blood vessels-like. (H) Elemental intensities for point 3 (blood vessel-like) shown in (E), showing it to be rich in carbon and nitrogen. (I) Elemental intensities for point 5 (bone matrix) shown in (E), showing an abundance of calcium, phosphorus, and iron, and absence of carbon and nitrogen. (J) Bone fragment placed in the SEM holder. (K) Micrograph showing a blood vessel-like embedded in the bone matrix, from the yellow region indicated in (J). (L) Close-up micrograph of the blood vessel-like shown in the red rectangle in (K). (M) Elemental intensities for point 3 (blood vessel-like) shown in (L), showing a high amount of carbon. (N) Elemental maps of the blood vessel-like shown in (L), indicating a high amount of carbon and nitrogen, these elements are absent in the surrounding bone matrix, which is composed mainly of calcium and phosphorus. (O–Q) Micrograph and EDS elemental maps of a bone margin in contact with rock matrix, the latter of which exhibits relatively higher amount of aluminum and absence of calcium, phosphorus, and iron. Full data for these EDS point analyses are presented in Data S1, S2.
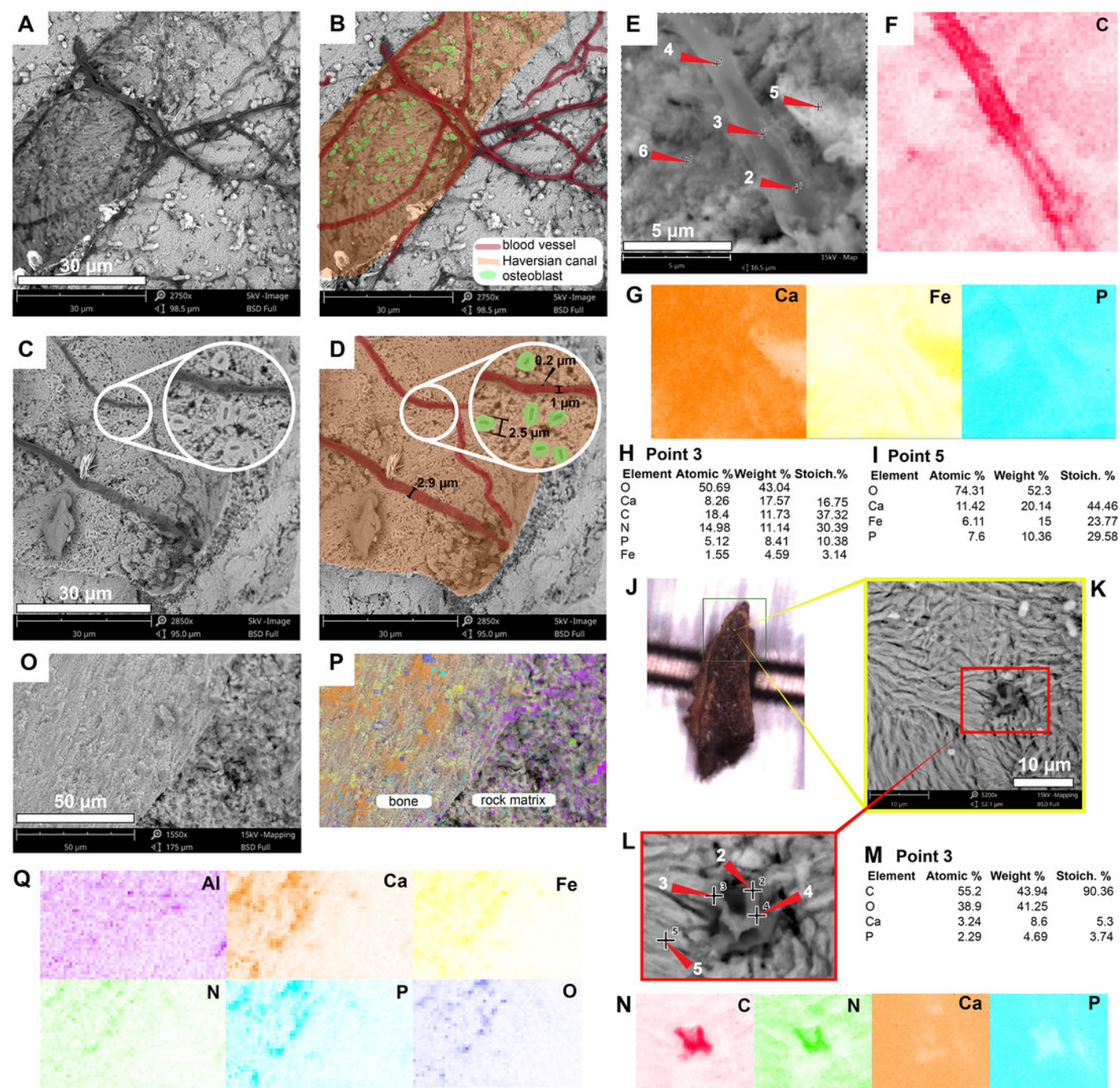
Figure 5

Figure 5. SEM/EDS analyses of podocnemidid indet. (UR-CP-0043) bone.

(A) Bone sample mounted in the SEM holder. (B–C) Micrograph and EDS element maps of one of the blood vessels-like embedded in the bone matrix, showing high amounts of carbon and nitrogen, a moderate amount of silicon; this differs from the bone matrix, which is dominated by calcium and phosphorus. (D) Elemental intensities for point 2 (blood vessel-like) shown in (B). (E) Elemental intensities for point 5 (bone matrix) shown in (B), showing a high amount of calcium and phosphorus. (F–G) Micrographs showing an osteocyte- and blood vessel-like 20 μm away from each other, both embedded in the bone matrix. (H) EDS element maps of the region shown in (F), the blood vessel-like exhibits high amounts of carbon and nitrogen, and the osteocyte-like is richer in iron but lacks significant carbon and nitrogen. (I) Elemental intensities for point 2 (blood vessel-like) shown in (F). (J) Elemental intensities for point 7 (osteocyte-like) shown in (F). (K) An isolated bone fragment after four days of demineralization, viewed under transmitted light microscopy (at 20x). (L) Close-up of the red rectangle region shown in (K), under polarized light microscopy (at 40x), showing darker osteocyte-like adjacent to where dendritic pyrolusite mats. (M) Close-up of the red rectangle region shown in (L) (at 100x), showing the dendritic pyrolusite and some of the osteocytes-like in detail. Full data for these EDS point analyses are presented in Data S1, S2.

A

B 5 6 2 3 4 10 µm 4900x 15kV - Mapping 10 µm 55.3 µm BSD Full 1

F 8 4 3 2 5 6 7 9 10 30 µm 1950x 15kV - Mapping 30 µm 139 µm BSD Full

G Haversian canal osteocyte

C Ca C N O P Si

H Ca C N Fe O P

D Point 2

Element	Atomic %	Weight %	Stoich. %
C	65.85	55.52	94.49
O	30.31	34.04	
Ca	1.52	4.28	2.19
Si	0.9	1.78	1.3
P	0.78	1.69	1.11

E Point 5

Element	Atomic %	Weight %	Stoich. %
O	69.85	49	
Ca	18.05	31.72	59.87
P	10.25	13.92	34

I Point 2

Element	Atomic %	Weight %	Stoich. %
C	40.53	31.91	51.49
N	30.89	28.36	39.23
O	21.27	22.31	
Ca	4.69	12.33	5.96
P	1.82	3.69	2.31

J Point 7

Element	Atomic %	Weight %	Stoich. %
O	63.45	40.83	
Fe	8.88	19.95	24.31
Ca	6.75	10.89	18.48
Al	9.36	10.15	25.6
Mn	4.32	9.54	11.81
P	4.05	5.05	11.09
Si	3.18	3.59	8.71

K 100 µm

L 50 µm

M Pyrolusite osteocytes 30 µm

Figure 6

Figure 6. SEM/EDS analyses of the extant turtle and chicken bones.

(A) Bone fragment of *Podocnemis lewyana* in the SEM holder. (B–C) Micrograph and EDS element maps of osteocytes embedded in the bone matrix, showing high amounts of carbon and nitrogen; this differ from the bone matrix, which is dominated by calcium and phosphorus. (D) Elemental intensities for point 3 (osteocyte) shown in (B). (E) Elemental intensities for point 4 (bone matrix) shown in (B). (F) Micrograph of one of the Volkmann canals and a blood vessel system in the sample of *P. lewyana*. (G) Close-up of the Volkmann canal wall and blood vessel system (outlined in red) *P. lewyana*. (H) Bone fragment of *Lepidochelys olivacea* in the SEM holder. (I) Micrograph of a region of the cancellous bone shown in the yellow rectangle in (H). (J–K) EDS composite (J) and individual elemental (K) analyses of the bone region shown in (I). (L) Elemental intensities for point 2 (blood vessel) shown in (I), showing high amount of carbon and nitrogen. (M) Elemental point values for point 5 (bone matrix) shown in (I), showing high amounts of calcium and carbon. (N) Bone fragment from a femur of *Gallus gallus* in the SEM holder. (O) Micrograph of the bone region shown in the yellow rectangle in (N), showing osteocytes embedded in the bone matrix. (P) EDS elemental maps of one of the osteocytes (in the red rectangle) shown in (O), showing a high amount of carbon within the cell. Full data for these point analyses are presented in Data S1, S2.

D Point 3

Element	Atomic %	Weight %	Stoich. %
C	55.48	39	79.16
Ca	12.22	28.65	17.43
O	29.92	28.02	
P	2.39	4.33	3.41

E Point 4

Element	Atomic %	Weight %	Stoich. %
Ca	19.56	39.47	30.72
O	36.34	29.28	35.2
N	22.41	15.8	
C	19.26	11.65	30.25
P	2.44	3.8	3.83

L Point 2

Element	Atomic %	Weight %	Stoich. %
C	53.67	43.52	69.25
O	22.49	24.29	
N	17.88	16.91	23.07
Ca	2.97	8.03	3.83
P	1.85	3.87	2.39

M Point 5

Element	Atomic %	Weight %	Stoich. %
Ca	24.58	46.58	34.36
C	41.17	23.38	57.56
O	28.47	21.54	
P	5.41	7.93	7.57